Schweizerischer Erdbebendienst
Service Sismologique Suisse
Servizio Sismico Svizzero
Servizi da Terratrembels Svizzer

Eidgenössische Technische Hochschule Zürich
Swiss Federal Institute of Technology Zurich

Linthal - Matt (SLTM2)

SITE CHARACTERIZATION REPORT

Clotaire MICHEL, Jan BURJANEK, Daniel ROTEN

Valerio POGGI, Carlo CAUZZI, Donat FÄH

Sonneggstrasse 5 CH-8092 Zürich Switzerland; E-mail: clotaire.michel@sed.ethz.ch

Last modified : November 5, 2013

Abstract

Two ambient vibration array measurements were performed in the middle of the narrow alpine valley of the Linth and close to the SLTM2 station in Linthal and allowed to derive important properties of the ground structure. Although doubt is remaining, the site is mostly behaving in the 1D fashion at SLTM2 site with a fundamental frequency of $1.34\,\mathrm{Hz}$.
The inversion of obtained dispersion curves allowed to conclude that this valley is hosting a relatively deep basin (around $250\,\mathrm{m}$ at station SLTM2). The filling is however made of stiff sediments with velocities from 600 up to $1100\,\mathrm{m/s}$. $V_{s,30}$ is found to be $620\,\mathrm{m/s}$, corresponding to class B in the Eurocode 8.

Contents

1 Introduction

The station SLTM2 (Linthal Matt) is part of the Swiss Strong Motion Network (SSMNet) in Glarus. It is the new location of the SLTM station in the frame of the SSMNet Renewal project. In order to avoid influence of the transformer house of SLTM, SLTM2 station was relocated in free-field and installed at some hundreds of meters. This project includes also the site characterization. The passive array measurement has been selected as a standard tool to investigate these sites. Two measurement campaigns were performed on 19th August 2010 and on 20th June 2011 in Linthal (Fig. 1), the first in the middle of the valley, $250\,\mathrm{m}$ away from the station SLTM and $170\,\mathrm{m}$ away from the station SLTM2 and the second at the SLTM2 site in order to characterize the narrow alpine valley under the SLTM2 station. The first array in the middle of the valley was larger (more space). This report presents the measurement setups, the results of the H/V analysis, especially the fundamental frequencies and of the polarization analysis and of the array processing of the surface waves (dispersion curves). Then, an inversion of these results into velocities in the different identified layers is performed. Finally, a discussion on the limitations of the technique for this site is done.

Canton	City	Location	Station code	Site type	Slope
Glarus	Linthal	Matt	SLTM2	Alpine valley	Flat

Table 1: Main characteristics of the study-site.

Figure 1: Picture of the site.

2 Experiment description

2.1 Ambient Vibrations

The ground surface is permanently subjected to ambient vibrations due to:

- natural sources (ocean and large-scale atmospheric phenomena) below $1\,\mathrm{Hz}$,
- local meteorological conditions (wind and rain) at frequencies around $1\,\mathrm{Hz}$,
- human activities (industrial machines, traffic...) at frequencies above $1\,\mathrm{Hz}$ [Bonnefoy-Claudet et al., 2006].

The objective of the measurements is to record these ambient vibrations and to use their propagation properties to infer the underground structure. First, the polarization of the recorded waves (H/V ratio) are used to derive the resonance frequencies of the ground layers. Second, the arrival time delays between stations is used to derive the velocity of surface waves at different frequencies (dispersion). The information (H/V, dispersion curves) is then used to derive the properties of the soil layers using an inversion process.

2.2 Equipment

For these 2 measurement campaigns 12 Quanterra Q330 dataloggers named NR01 to NR12 and 14 Lennartz 3C 5 s seismometers were available (see Tab. 2). Each datalogger can record on 2 ports A (channels EH1, EH2, EH3 for Z, N, E directions) and B (channels EH4, EH5, EH6 for Z, N, E directions). The time synchronization was ensured by GPS. The sensor are placed on a metal tripod in a $20\,\mathrm{cm}$ hole, when possible, for a better coupling with the ground.

Digitizer	**Model**	**Number**	**Resolution**
	Quanterra Q330	12	$24\,\mathrm{bits}$
Sensor type	**Model**	**Number**	**Cut-off frequency**
Velocimeter	Lennartz 3C	14	$0.2\,\mathrm{Hz}$

Table 2: Equipment used.

2.3 Geometry of the arrays

For the first campaign, two array configurations were used, for a total of 4 rings of 10, 25, 60 and $120\,\mathrm{m}$ radius around a central station. The first configuration includes the 3 inner rings with 14 sensors; the second configuration includes the 2 outer rings with 12 sensors. The minimum inter-station distance and the aperture are therefore 10 and $120\,\mathrm{m}$ and 60 and $240\,\mathrm{m}$, respectively.

For the second campaign, one configuration with 3 rings of 7, 15 and $30\,\mathrm{m}$ around a central station was performed (14 sensors). The minimum inter-station distance and the aperture are therefore 7 and $60\,\mathrm{m}$

The experimental setups are displayed in Fig. 2. The final usable datasets are detailed in section 3.2.

Figure 2: Geometry of the arrays.

2.4 Positioning of the stations

The sensor coordinates were measured using a differential GPS device (Leica Viva), including only a rover station. The differential GPS computation is done on the fly using a GSM link with Swisstopo. It allows positioning with an accuracy of about 3 cm on the Swissgrid.

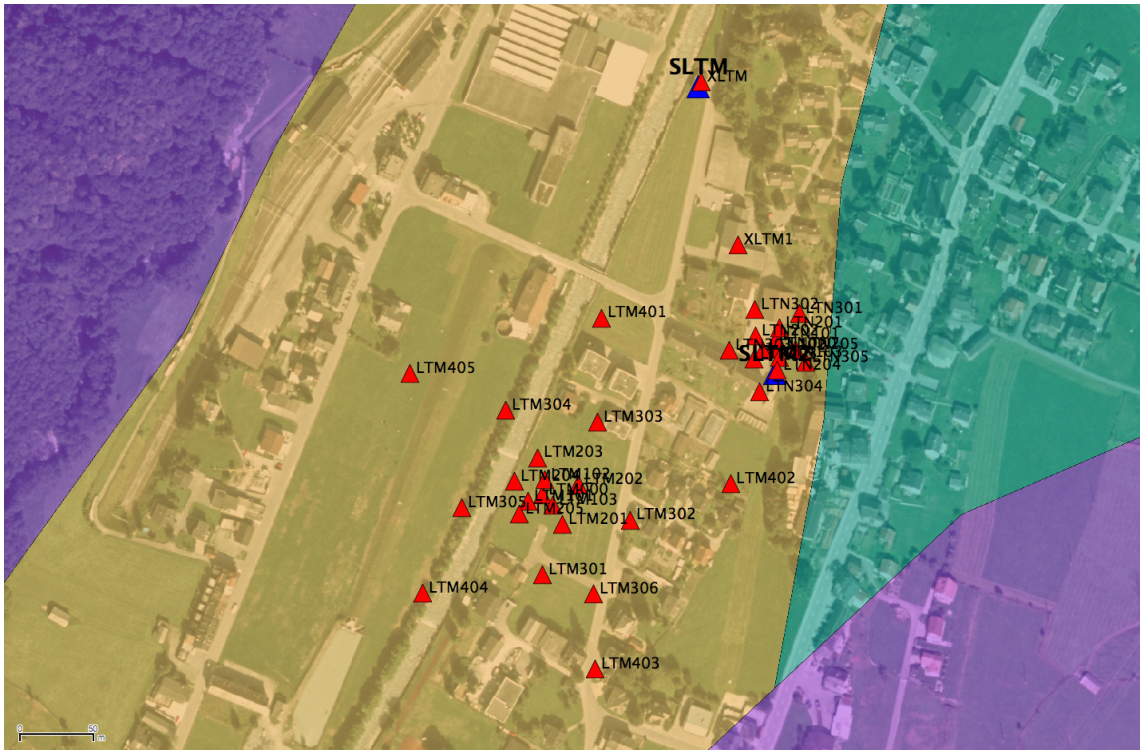

Figure 3: Location of the arrays and the SSMNet stations in the narrow Linth valley.

3 Data quality

3.1 Usable data

The largest time windows were extracted, for which all the sensors of the array were in position and the GPS synchronization was ensured. The characteristics of the datasets are detailed in Tab. 3.
During the first campaign, station NR04 (point LTM304) did not write data on the Baler that was not clean. Compared to the classically used geometry, an additional point (LTM306) has been added during the second measurement close to the car.

3.2 Data processing

The data were first converted to SAC format including in the header the coordinates of the point (CH1903 system), the recording component and a name related to the position. The name is made of 3 letters characterizing the location (LTM for the first campaign, LTN for the second), 1 digit for the ring and 2 more digits for the number in the ring. The response of the sensor was not corrected and the values (in counts) were not converted to $\mathrm{m/s}$.

Dataset	**Starting Date**	**Time**	**Length**	F_s	**Min. inter-distance**	**Aperture**	**# of points**
LTM 1	2010/08/19	08:39	111 min	200 Hz	10 m	120 m	13
LTM 2	2010/08/19	12:15	107 min	200 Hz	60 m	240 m	11
LTN	2011/06/20	12:50	99 min	200 Hz	7 m	60 m	14

Table 3: Usable datasets.

4 H/V processing

4.1 Processing method and parameters

In order to process the H/V spectral ratios, several codes and methods were used. The classical H/V method was computed using the Geopsy `http://www.geopsy.org` software. It averages the ratio of the smoothed Fourier Transform of selected time windows. Tukey windows (cosine taper of 5% width) of $50\,\mathrm{s}$ long overlapping by 50% were selected. The smoothing was done using the Konno and Ohmachi [1998] procedure with a b value of 80. The classical method computed using the method of Fäh et al. [2001] was also performed

Moreover, the time-frequency analysis method [Fäh et al., 2009] was used to estimate the ellipticity function more accurately using the Matlab code of V. Poggi. In this method, the time-frequency analysis using the Wavelet transform is computed for each component. For each frequency, the maxima in time (10 per minute with at least $0.1\,\mathrm{s}$ between each) in the TFA are determined. The Horizontal to Vertical ratio of amplitudes for each maxima is then computed and statistical properties for each frequency are derived. The used wavelet is a Cosine wavelet with parameter 9. The mean of the distribution for each frequency is kept. For the sake of comparison, the time-frequency analysis by Fäh et al. [2001], based on the spectrogram, was also used, as well as the wavelet-based TFA coded in Geopsy.

The ellipticity extraction using the Capon analysis [Poggi and Fäh, 2010] (see section on array analysis) was also performed.

Method	Freq. band	Win. length	Anti-trig.	Overlap	Smoothing
Standard H/V Geopsy	$0.5-20\,\mathrm{Hz}$	$50\,\mathrm{s}$	No	50%	K&O 80
Standard H/V D. Fäh	$0.5-20\,\mathrm{Hz}$	$30\,\mathrm{s}$	No	75%	?
H/V TFA Geopsy	$0.5-20\,\mathrm{Hz}$	Morlet m=8 fi=1	No	-	?
H/V TFA D. Fäh	$0.5-20\,\mathrm{Hz}$	Specgram	No	-	?
H/V TFA V. Poggi	$0.5-20\,\mathrm{Hz}$	Cosine wpar=9	No	-	No

Table 4: Methods and parameters used for the H/V processing.

4.2 Results

First campaign The results show a relatively homogeneous region regarding especially the right flank of the ellipticity function. The peak is however not well defined around $0.8-0.9\,\mathrm{Hz}$ (Fig. 4) for all points except LTM404 (lower frequency peak around $0.6\,\mathrm{Hz}$) and LTM405 (higher frequency peak around $0.9\,\mathrm{Hz}$). Considering the shape of the H/V ratios, the actual peak may be at much higher frequency, up to $1.4\,\mathrm{Hz}$ if one only consider the right flank of the ellipticity. Using the Time-Frequency analysis does not change much the picture (Fig. 4 bottom). In both computations, the central point LTM000 has higher amplitudes in the ellipticity function but the peak is not changed. The comparison of all available methods is displayed on point LTM101 (Fig. 7), in which the classical methods were arbitrary divided by $\sqrt{2}$. The matching above the resonance frequency is almost perfect except smoothing issues.

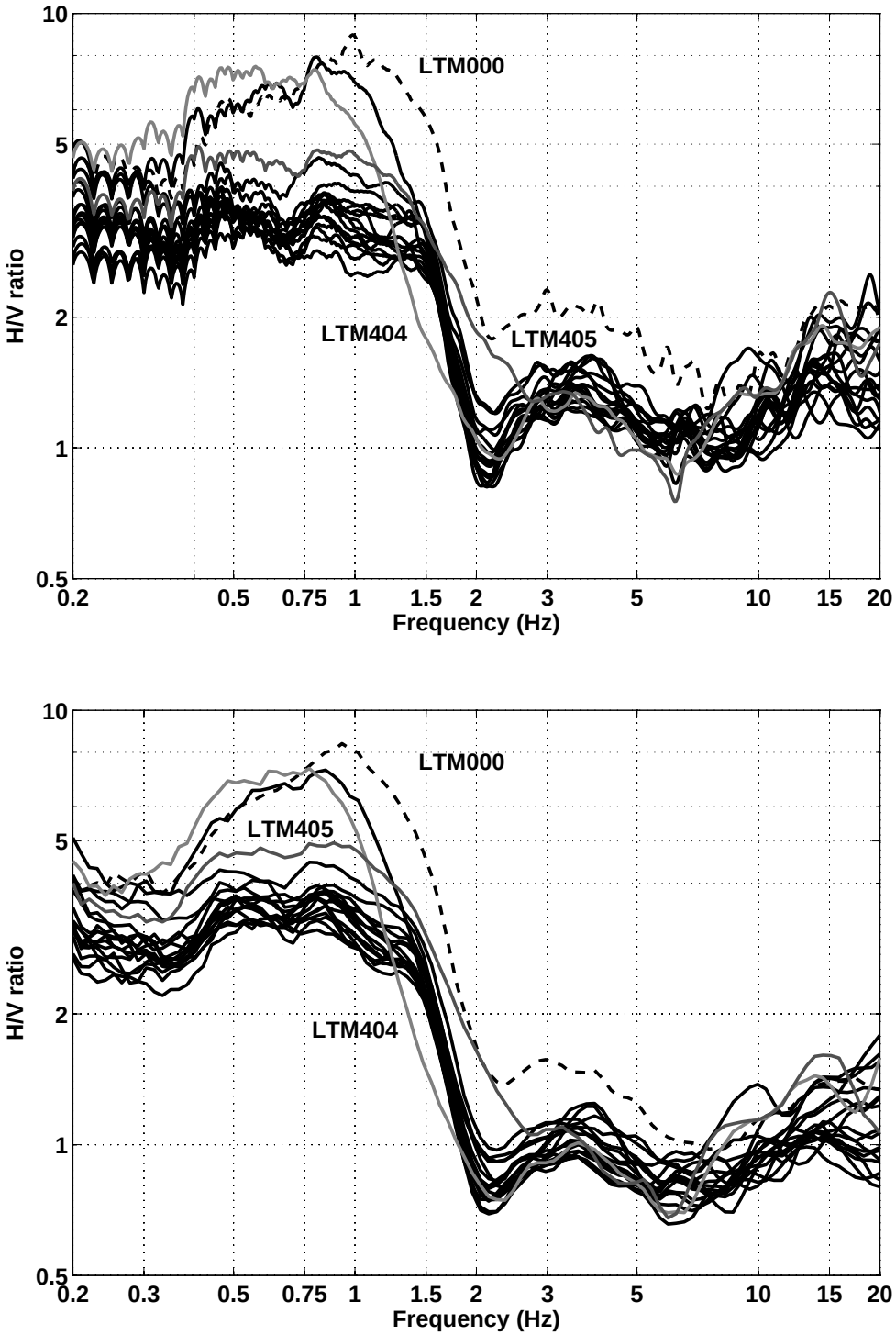

Figure 4: H/V spectral ratios using the standard method (Geopsy - top) and the TFA method (code V: Poggi - bottom) for the first campaign.

Second campaign For the second campaign, the H/V plots are again homogenous except for station LTN303 that was probably too close to an underground tube. The vertical motion for this station is very affected and should not be used in the array analysis. Station LTN204, the closest to SLTM2 seems also affected by the station pot or the loose soil from the construction of the pot and the results are deviating from what is awaited. The spectra are different from the others and should not be used. Station LTN205, in the slope, shows an additional a peak at $12\,\mathrm{Hz}$.

The comparison between both measurement campaigns (Fig. 6) shows an identical ellipticity peak and right flank, up to $3\,\mathrm{Hz}$. Looking at the H/V ratios of the second campaign, the hypothesis of a $0.8 - 0.9\,\mathrm{Hz}$ fundamental peak vanishes, a peak between 1 and $1.4\,\mathrm{Hz}$ seems more realistic, the ratios below this value being untrusted due to a too low energy. Between 3 and $8\,\mathrm{Hz}$, the H/V ratio are consistently different, both from H/V and 3CFK analysis. At higher frequencies, the H/V ratios of the different recording points are no more correlated.

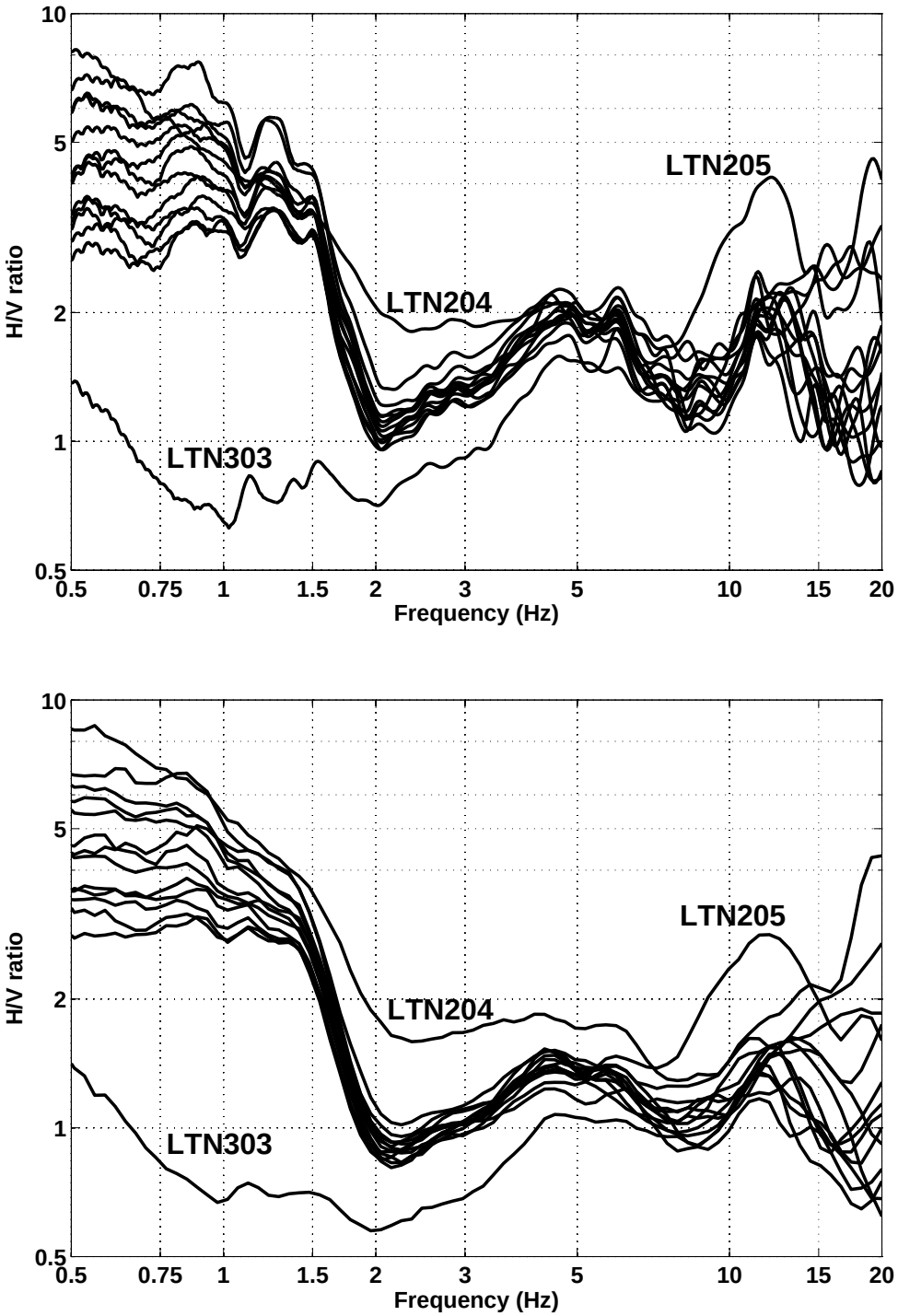

Figure 5: H/V spectral ratios using the standard method (Geopsy - top) and the TFA method (code V: Poggi - bottom) for the second campaign.

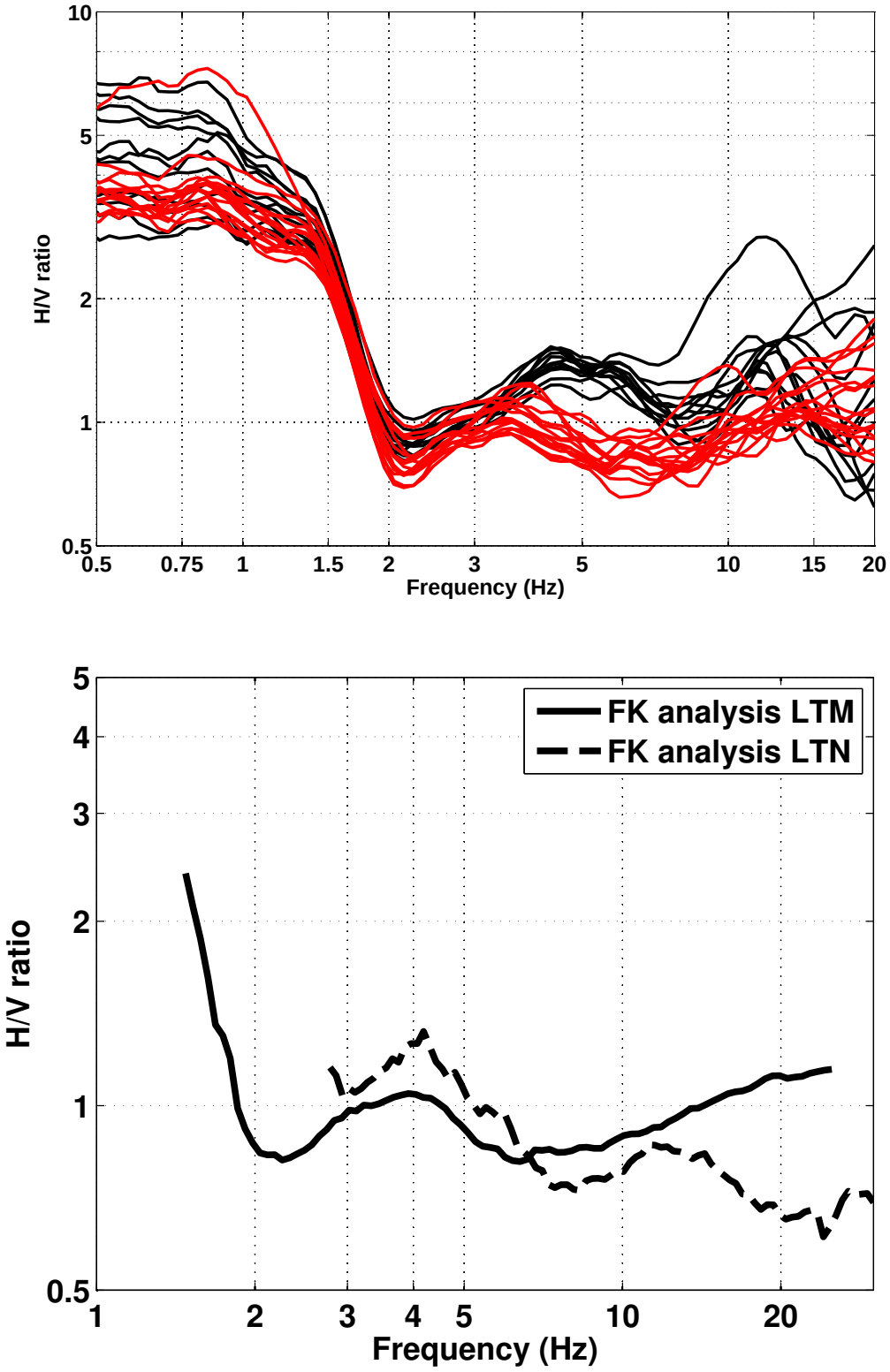

Figure 6: Top: Selected H/V spectral ratios using the TFA method for the first (black) and second (red) campaigns. Bottom: Comparison of the ellipticity from 3CFK analysis between both campaigns.

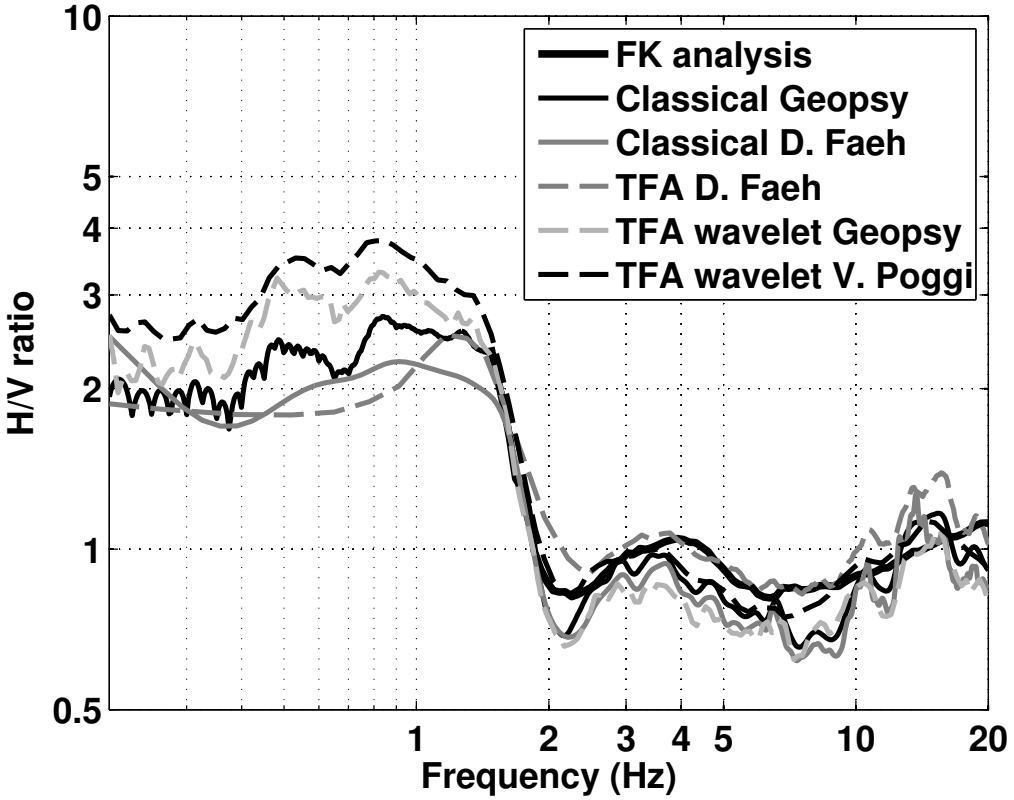

Figure 7: H/V spectral ratios using all available methods at point LTM101 (central part of the first array). Classical methods were divided by $\sqrt{2}$.

5 2D or 1D resonance?

In the case of such a narrow sedimentary valley, it is relevant to wonder if the ellipticity function found using the H/V method is related to 1D or 2D resonance. H/V first showed that the both tested sites in the valley had a similar ellipticity function, whereas the second one is closer to the edge of the valley, which is in favor of a 2D resonance. However, considering the difficulty to pick the peaks on these H/V curves and the fact that none of the point is really close to the valley edge, it could still be representative of a 1D resonance. In order to investigate this in more details, comparisons with other valleys using the valley shape and the velocity contrast (from data obtained at the end of this report) are performed. Then a polarization analysis is performed to highlight eventual 2D normal modes of the valley.

5.1 Information from the valley shape and velocity contrast

Bard and Bouchon [1985] proposed a method to predict the observation of 2D resonance in valleys based on the valley shape and the velocity contrast. The valley shape is not very well defined, but one can assume the half-depth width of the valley $2w$ as defined by Roten et al. [2006] to be around $450\,\mathrm{m}$, with a minimum value of $400\,\mathrm{m}$ (half of the valley width) and a maximum value of $800\,\mathrm{m}$ (valley width). Therefore the shape ratio $h/2w$ is most probably around 0.55, but for sure between 0.25 and 0.75. The velocity contrast, however, is low compared to the Rhone valley, considering the array results. It could range between 1.5 and 3.5, and is most probably around 2, but the bedrock velocity is poorly constrained. Fig. 8 shows the domains of 1D and 2D resonance and the Linthal site. The site is located at the border of the domain so that no clear 2D resonance is expected as in the Vetroz site though it may occur.

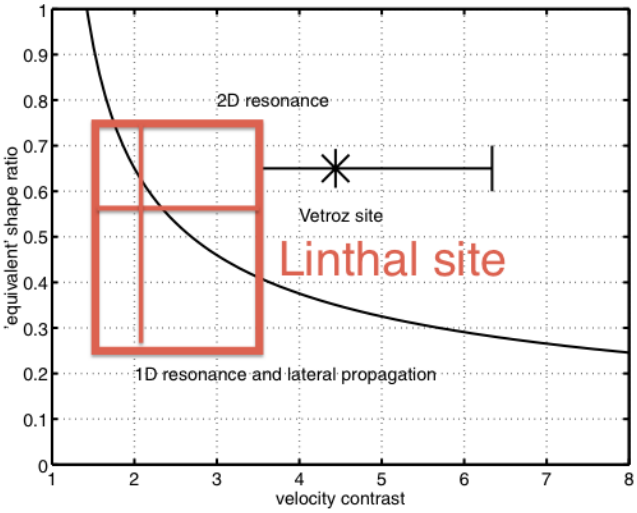

Figure 8: 1D/2D resonance domain for the Linthal site, after Roten et al. [2006]

5.2 Polarization analysis

A polarization analysis [Burjánek et al., 2010] was performed on long-term recordings (station XLTM1) during the night in the cellar of the Electricity company headquarters, hosting the SLTM2 station, located $100\,\mathrm{m}$ downstream. It shows a clear directionality at the resonance frequency $1.15\,\mathrm{Hz}$, that is following the direction of the valley 31°N (Fig. 9 top left). The dip at this frequency is 0 confirming this represents the 2D SH fundamental mode (Fig. 9 top right). At this frequency value, the ellipticity of the particle motion shows a minimum characteristic of the SH mode (Fig. 9 bottom). Moreover, around $2.5\,\mathrm{Hz}$, a peak in the polarization is found in the direction perpendicular to the valley 111°N (Fig. 9 top left). It is dipping of 30°, as expected in the valley side (Fig. 9 top right). It shows that 2D resonance occurs at the XLTM1 site.

However, the same analysis was performed on the array data LTN and shows a weak polarization in the direction of the slope of the alluvial fan, not in the direction of the valley. For the LTM array, no coherent polarization can be found.

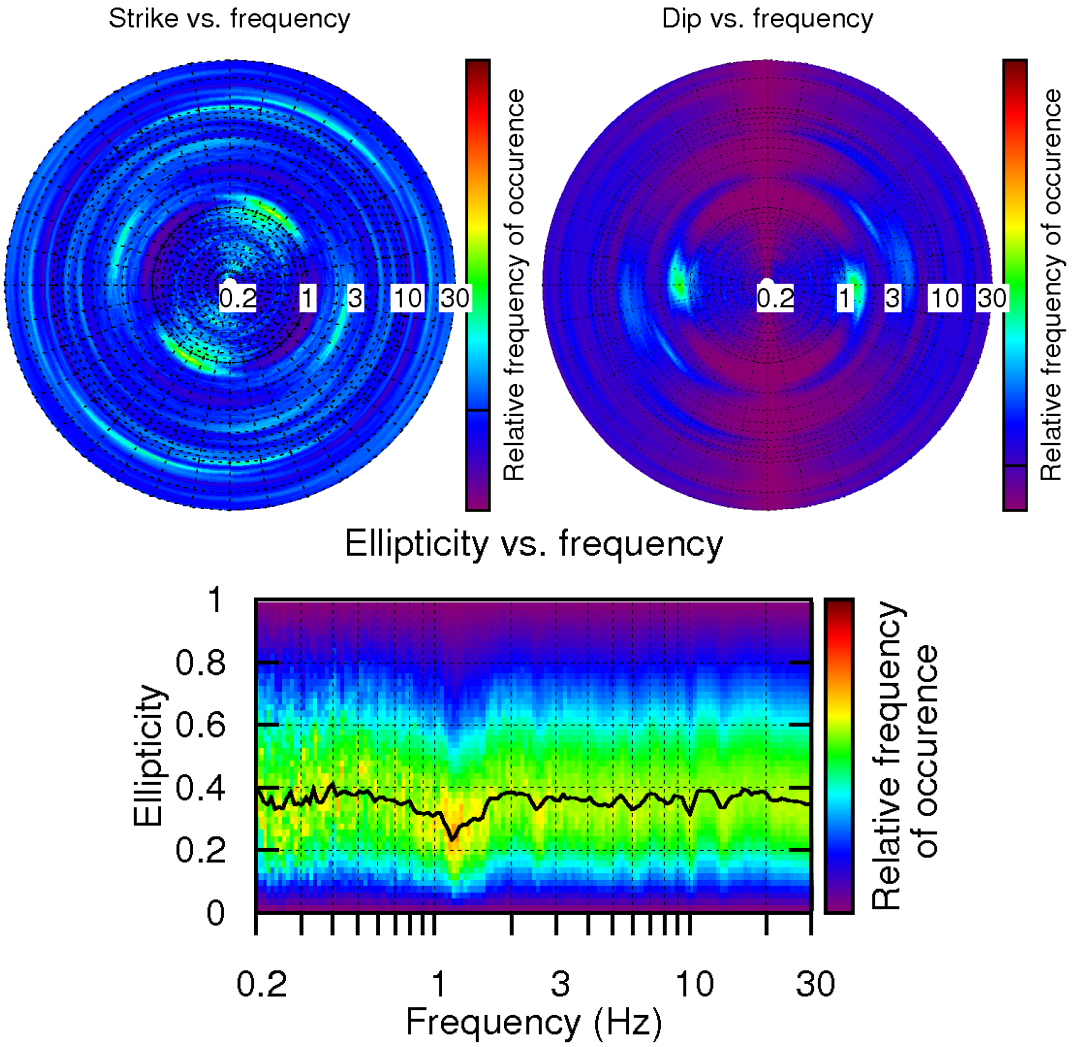

Figure 9: Polarization analysis of the night recording XLTM1. Top left: strike; Top right: dip; Bottom: Ellipticity.

5.3 Conclusion

Another source of information is the empirical spectral modeling (ESM) amplification function of the station, computed using earthquake recordings [Edwards et al., 2013]. This function looks like a 1D transfer function with clear resonance peaks, without flattening due to edge-generated surface waves. Moreover, the fundamental peak frequency at $1.34\,\mathrm{Hz}$ is compatible with the H/V curve of the closest recordings within the array. Finally, it seems that the H/V curves are not affected much by 2D resonance, but the peak value is difficult to obtain with accuracy and the previously given values may be biased. At station SLTM2, the value $1.34\,\mathrm{Hz}$ should therefore be used. In order to confirm this, the 1D transfer function of SLTM site should be checked as well. Since the polarization analysis showed the motion was 2D at this site, we should also see flattening due to edge-generated surface-waves. As a conclusion for SLTM2, the site is probably not affected by a 2D resonance of the whole Linth valley but 2D effects linked to the alluvial fan it sits on may occur.

6 Array processing

6.1 Processing methods and parameters

The vertical components of the arrays were processed using the FK and the High-resolution FK analysis [Capon, 1969] using the Geopsy `http://www.geopsy.org` software. Large time windows were considered (500T) because it gave better results.

Moreover, a 3C array analysis [Fäh et al., 2008] was also performed using the array_tool_3C software software [Poggi and Fäh, 2010]. It allows to derive Rayleigh and Love modes. The results of computations of both datasets were assembled to estimate the dispersion curves.

Method	Set	Freq. band	Win. length	Anti-trig.	Overlap	Grid step	Grid size	# max.
HRFK 1C	LTM1	$1-23\,\mathrm{Hz}$	$500T$	No	50%	0.001	0.3	5
HRFK 1C	LTM2	$1-23\,\mathrm{Hz}$	$500T$	No	50%	0.001	0.3	5
HRFK 3C	LTM1	$1-25\,\mathrm{Hz}$	Wav. 10	No	50%	300	3500	5
			Tap. 0.2			m/s	m/s	
HRFK 3C	LTM2	$1-25\,\mathrm{Hz}$	Wav. 10	No	50%	300	3500	5
			Tap. 0.2			m/s	m/s	
HRFK 1C	LTN	$1.5-30\,\mathrm{Hz}$	$300T$	No	50%	0.005	0.6	5
HRFK 3C	LTN	$2-30\,\mathrm{Hz}$	Wav. 10	No	50%	200	2000	5
			Tap. 0.2			m/s	m/s	

Table 5: Methods and parameters used for the array processing.

6.2 Obtained dispersion curves

First campaign LTM The first mode (Rayleigh) in the 1C FK analysis could be picked between 2 and $20\,\mathrm{Hz}$ (Fig. 10). At $6\,\mathrm{Hz}$, a higher modes seems to start toward high frequencies but it is not energetic enough to be used. The velocities are high from $1800\,\mathrm{m/s}$ at $2\,\mathrm{Hz}$ down to $520\,\mathrm{m/s}$ at $20\,\mathrm{Hz}$.

Using the 3C analysis (Fig. 11), both fundamental Rayleigh and Love modes can be picked from 2 to $23\,\mathrm{Hz}$ (the portion between 2 and $2.7\,\mathrm{Hz}$ being outside the resolution limits) and from 2.5 to $17\,\mathrm{Hz}$, respectively. The vertical and radial components show the Rayleigh fundamental mode, a higher mode can be guessed but is not picked (Fig. 11). In the transverse direction, first and second datasets do not lead to the same results. The fundamental Love mode is therefore picked independently from the two subsets (Fig. 11). More generally, at low frequency, the velocity increase corresponding to the interface with the bedrock is not clear for both vertical and transverse components. It can be argued that the array limits can explain this, but, in this case, the lateral variability of this interface (dipping probably steeply below the sediments) is probably the most important reason. However, this does not affect the higher frequencies for Rayleigh mode, but it does for Love mode.

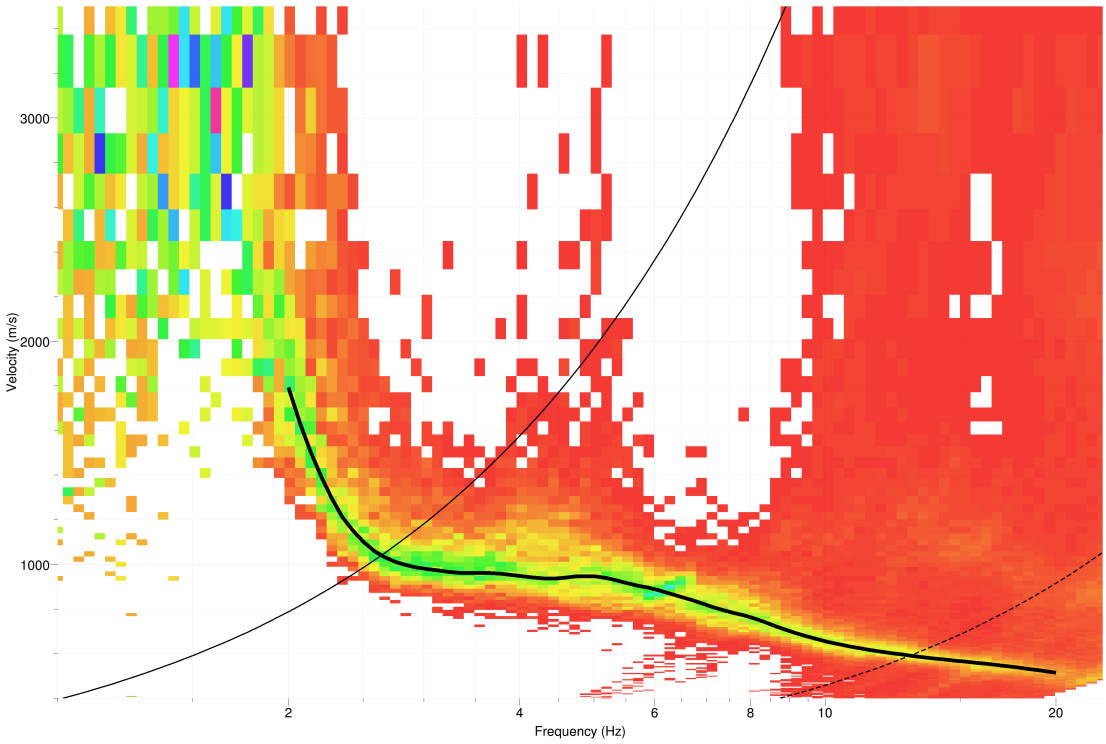

Figure 10: Dispersion curve obtained from the 1C array analysis of the LTM array.

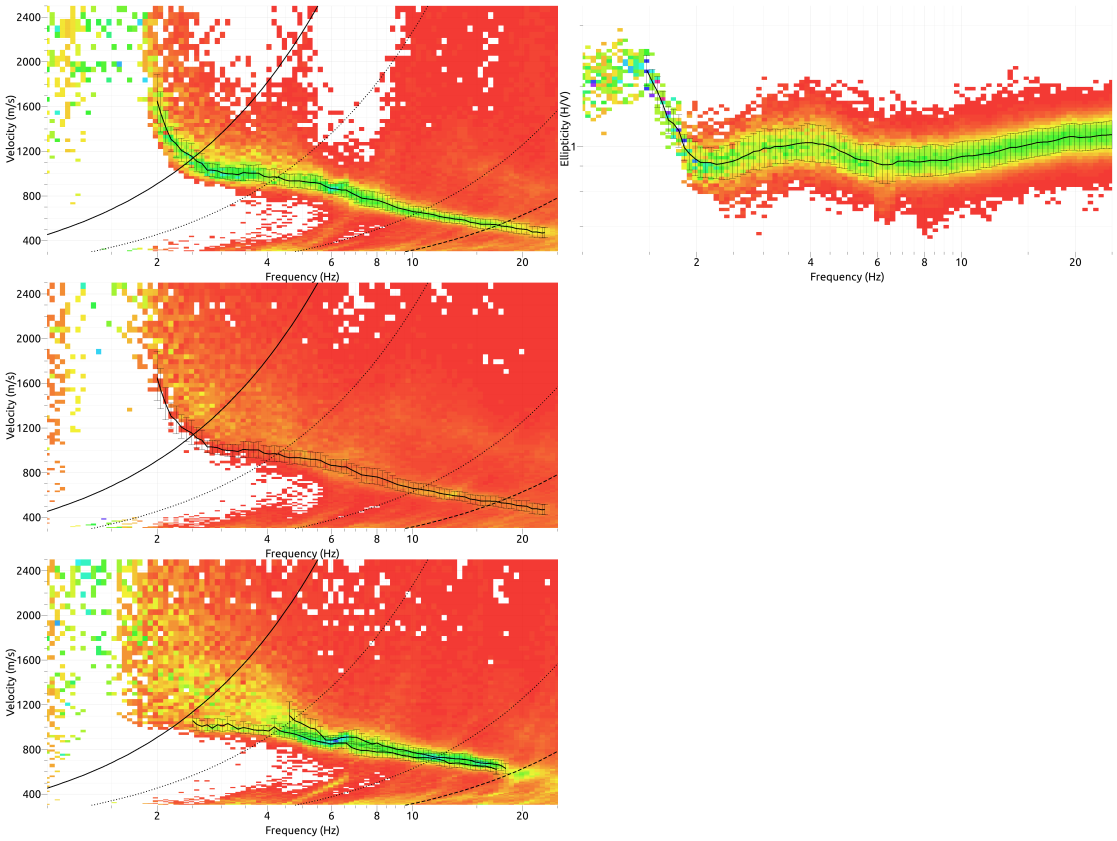

Figure 11: Results from the 3C analysis of array LTM by merging the maxima of the first and second dataset. Picking of the Love fundamental mode was made independently for each dataset.

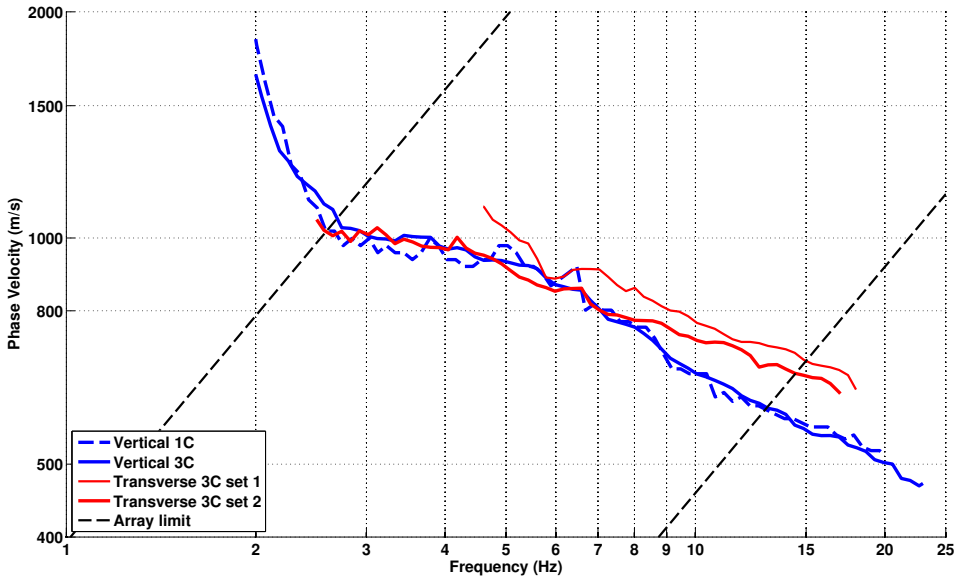

Figure 12: Comparison of obtained dispersion curves using 1C and 3C analyses for the LTM array.

Second campaign LTN In the 1C HRFK analysis (Fig. 13), only Rayleigh fundamental mode is picked. Bumps can be observed in the dispersion curve at 8.3 and 14.7 Hz. Looking at the spectra they are due to industrial undamped peaks at the same frequencies, coming from the East-South-East according to the FK analysis. It would correspond to a small factory on the main road. These machines are forcing the ground into vibration so that all sensors are in phase at this frequency, explaining that the apparent velocity increases.

In the 3C HRFK analysis (Fig. 14), Rayleigh mode can as well be clearly picked. Above 20 Hz, a large decrease in the velocity appears, that is not picked with the 1C analysis (Fig. 15). A higher Rayleigh mode is picked as well on the radial component. The transverse component, however, is much less clear. Only a short chunk of the fundamental Love mode is picked.

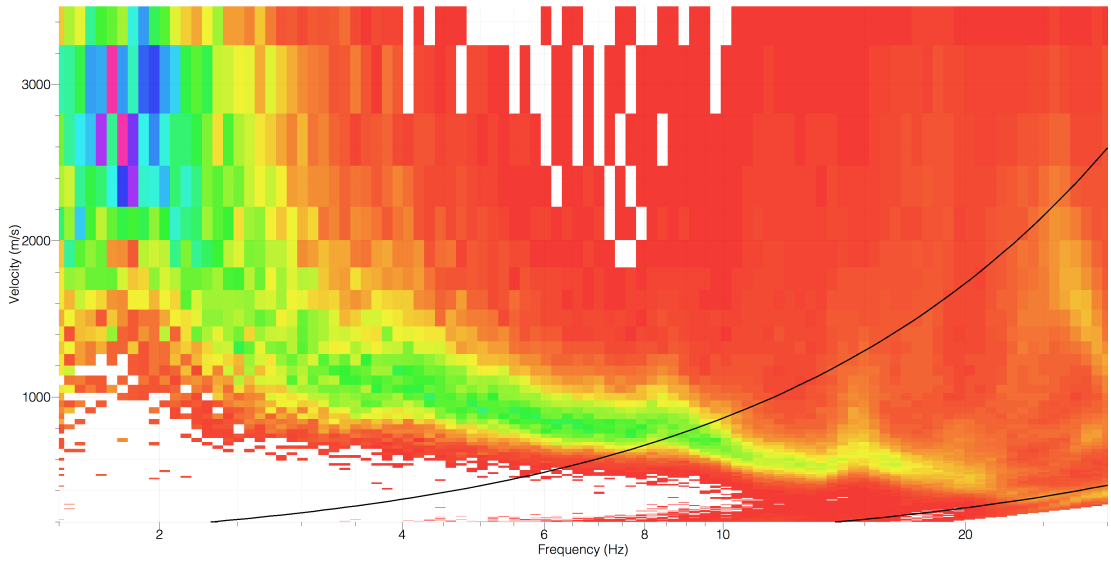

Figure 13: Histograms obtained from the 1C analysis of the second experiment.

Comparison of both campaigns When comparing the derived curves from the first and the second campaign (Fig. 16), two differences are noted on the Rayleigh mode: At low frequency, the velocity increase corresponding to the bedrock interface occurs at higher frequency for the LTN than for the LTM arrays. This is coherent with the fact that the LTN array is located closer to the edge of the basin than LTM but it occurs out of the array limit and may be strongly biased. The second difference is above 20 Hz, where a strong velocity decrease occurs. It may however be an artifact, since no peak related to such a velocity contrast is observed on the H/V curve. For the Love mode, the picked part does not seem very relevant, though not dramatically different. Finally, and after extensive testing in the inversion, the LTN dispersion curves are discarded since they are less reliable than the LTM and not significantly different.

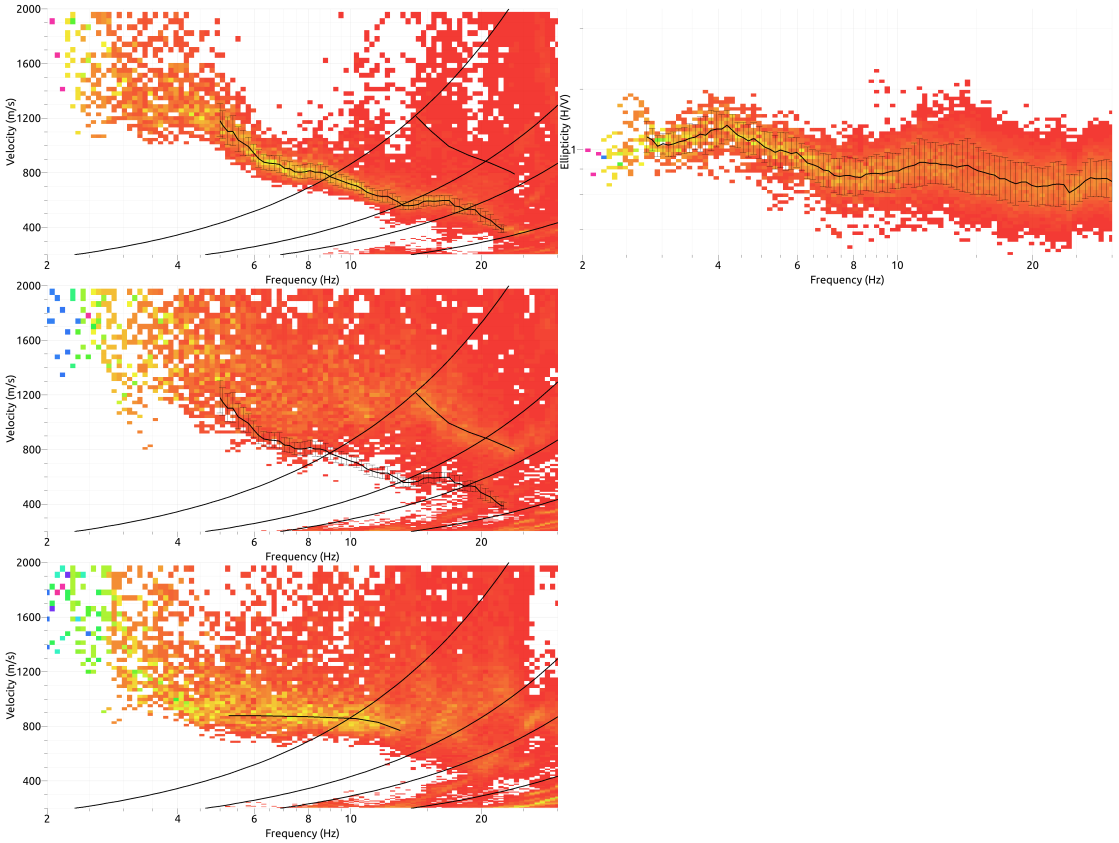

Figure 14: Results from the 3C analysis of array LTN.

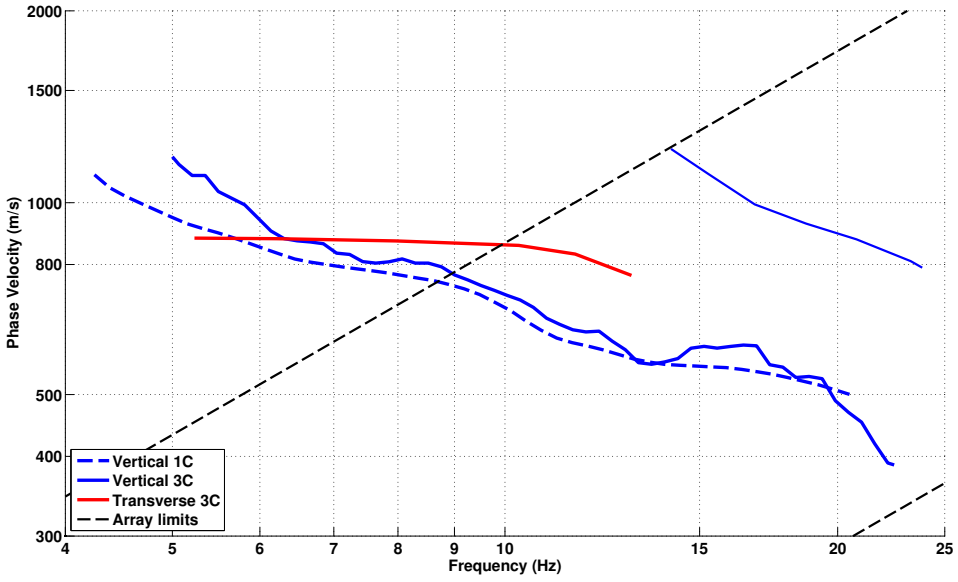

Figure 15: Comparison of obtained dispersion curves using 1C and 3C analyses for second campaign.

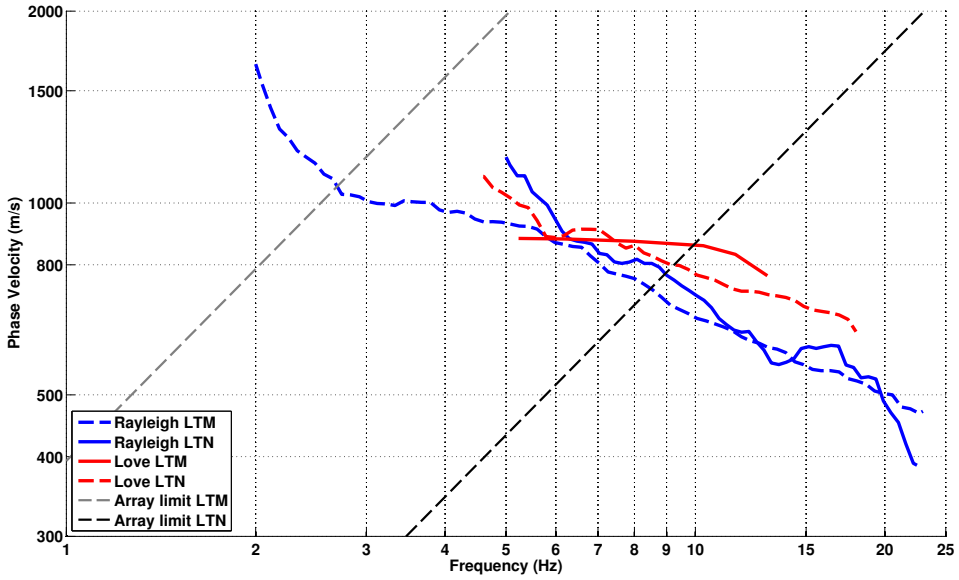

Figure 16: Comparison of obtained dispersion curves on the first and second campaign.

7 Inversion and interpretation

7.1 Inversion

For the inversion, the Love and Rayleigh fundamental modes dispersion curves of the first measurement campaign without standard deviation to avoid different weighting as well as the ellipticity between 1.4 and $19\,\mathrm{Hz}$ from point LTN103 and the ellipticity peak at $1.34\,\mathrm{Hz}$ (peak on ESM amplification) were used as simultaneous targets. The assumption below this is that SH fundamental peak and H/V peak are the same, which is quite simplistic but the only constraint we have on the bedrock. Point LTN103 was chosen because it was the closest to station SLTM2 with good quality (quality of LTN204 is poor). It also means that this inversion targets the velocity profile below station SLTM2, not at the centre of the array. A weight of 0.2 was assigned to the ellipticity curve and the ellipticity peak. All dispersion curves were resampled using 50 points between 1 and $25\,\mathrm{Hz}$ in log scale.

The inversion was performed using the Improved Neighborhood Algorithm (NA) Wathelet [2008] implemented in the Dinver software. In this algorithm, the tuning parameters are the following: Ns_0 is the number of starting models, randomly distributed in the parameter space, Nr is the the number of best cells considered around these Ns_0 models, Ns is the number of new cells generated in the neighborhood of the Nr cells (Ns/Nr per cell) and It_{max} is the number of iteration of this process. The process ends with $Ns_0 + Nr * \frac{Ns}{Nr} * It_{max}$ models. The used parameters are detailed in Tab. 6.

It_{max}	Ns_0	Ns	Nr
500	10000	100	100

Table 6: Tuning parameters of Neighborhood Algorithm.

During the inversion process, low velocity zones were not allowed. The Poisson ratio was supposed uniform in each layer (free parameter in the range 0.2-0.4) and the density was supposed equal to $2000\,\mathrm{kg/m^3}$ except for the lowest layers ($2400\,\mathrm{kg/m^3}$). The number of layers was modified increasingly until a sufficient exploration of the parameter space. 4 layers are enough to explain the targets (dispersion and ellipticity), but more layers are used to smooth the obtained results and better explore the parameter space. 5 independent runs of 4 different parametrization schemes were performed: 4, 5 and 6 layers over a half space with free depths and 13 and 16 layers with fixed depths. For further elaborations, the best models of these 25 runs were selected (Fig. 20).

The results (Fig. 17, Fig. 18 and Fig. 19) show a thin layer at the surface of 2 to $3\,\mathrm{m}$ depth with low velocity (200 to $300\,\mathrm{m/s}$). Down to $20\,\mathrm{m}$ depth, the velocity remains between 600 and $700\,\mathrm{m/s}$ (already compacted sediments) but then starts to increase linearly with depth down to $60\,\mathrm{m}$ depth where it reaches velocities around $1100\,\mathrm{m/s}$. This velocity seems to stay constant until the bedrock. The bedrock depth is estimated between 230 and $260\,\mathrm{m}$ using the ellipticity information. The velocity in this lowest layer is not constrained and found between 2400 and $2900\,\mathrm{m/s}$.

When comparing to the targets (Fig. 17, all curves are well represented by the inverted models.

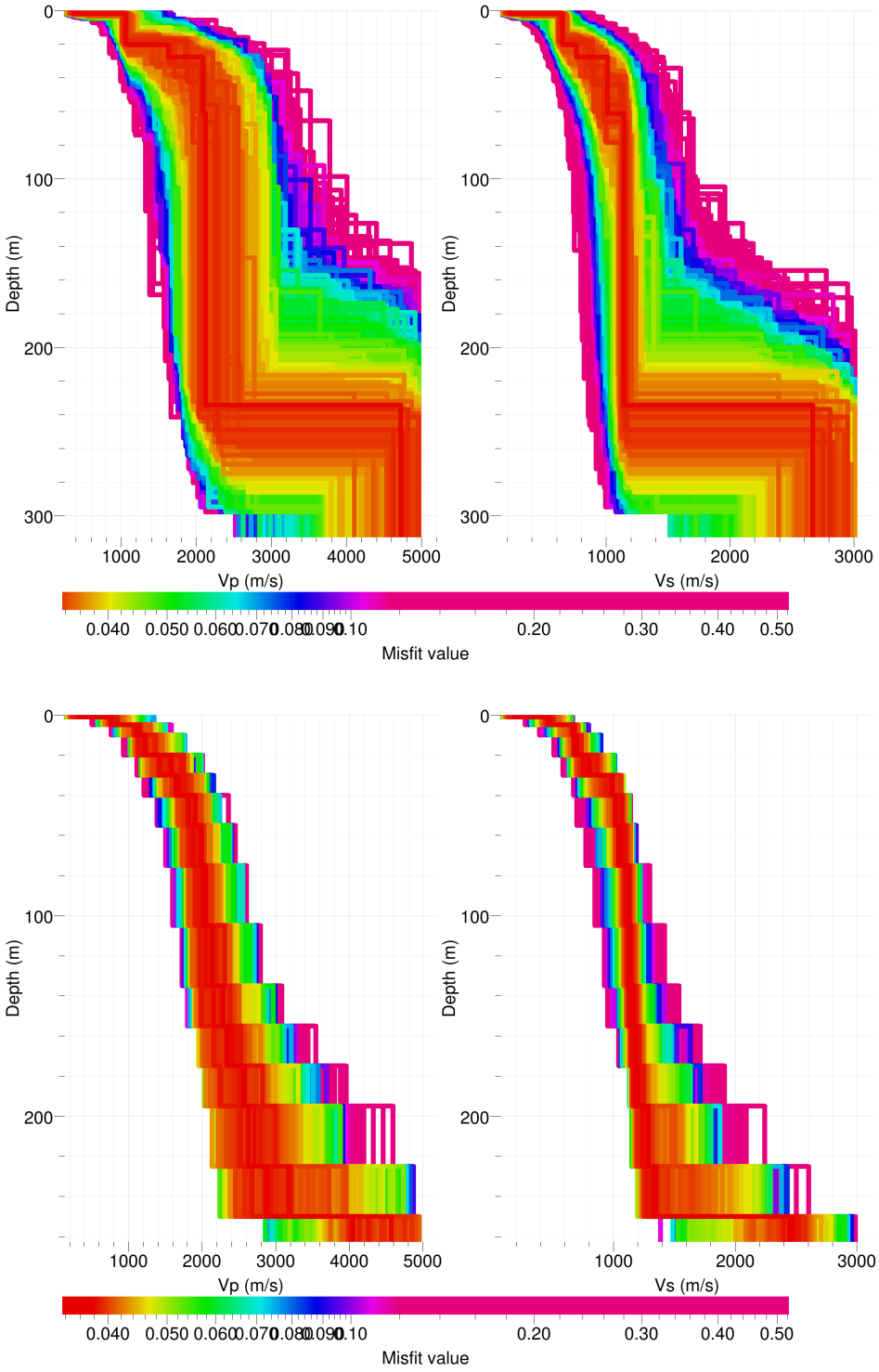

Figure 17: Inverted ground profiles in terms of V_p and V_s; top: free layer depth strategy; bottom: fixed layer depth strategy.

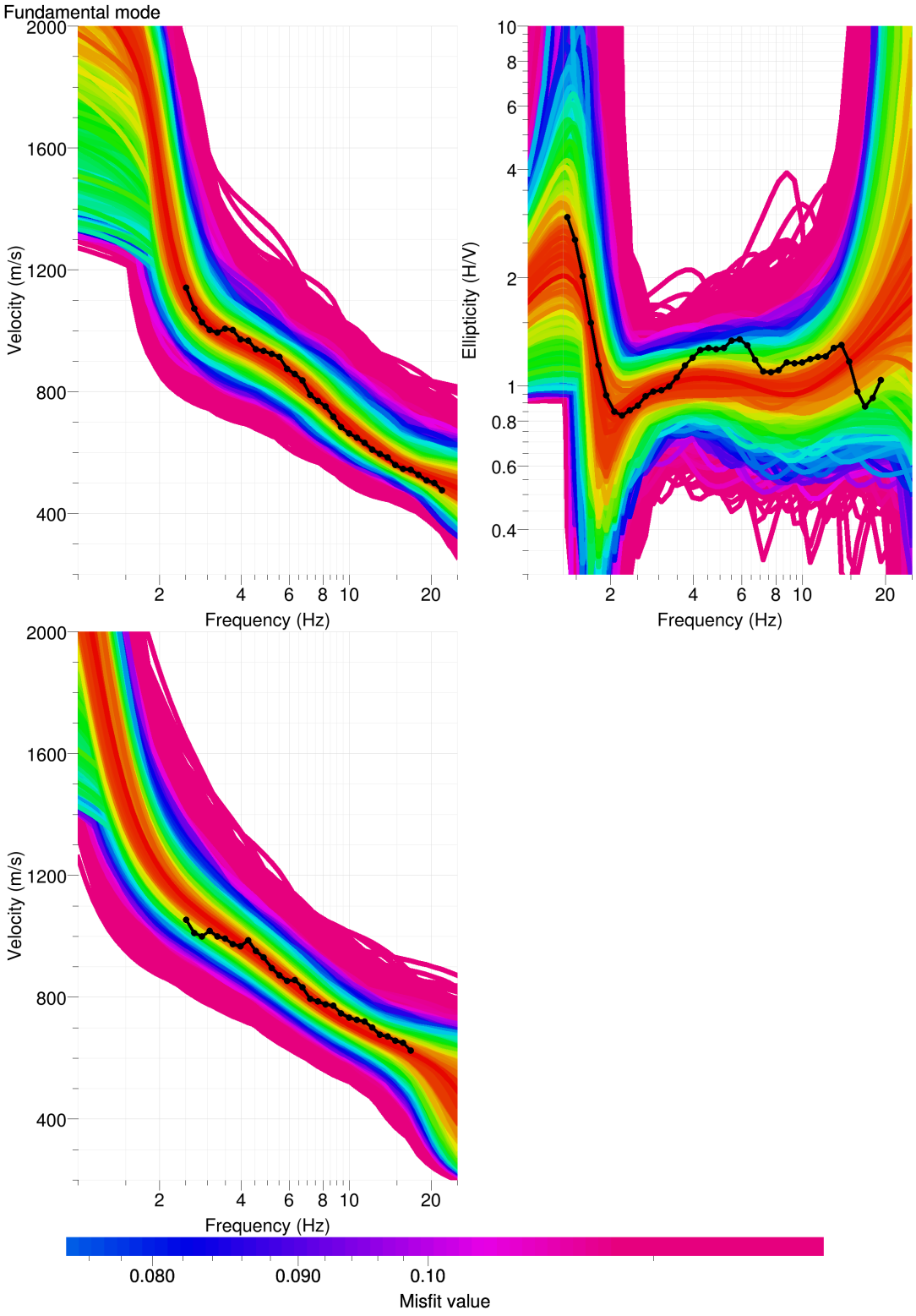

Figure 18: Comparison between inverted models and measured Rayleigh and Love modes and corresponding ellipticity, free layer depth strategy.

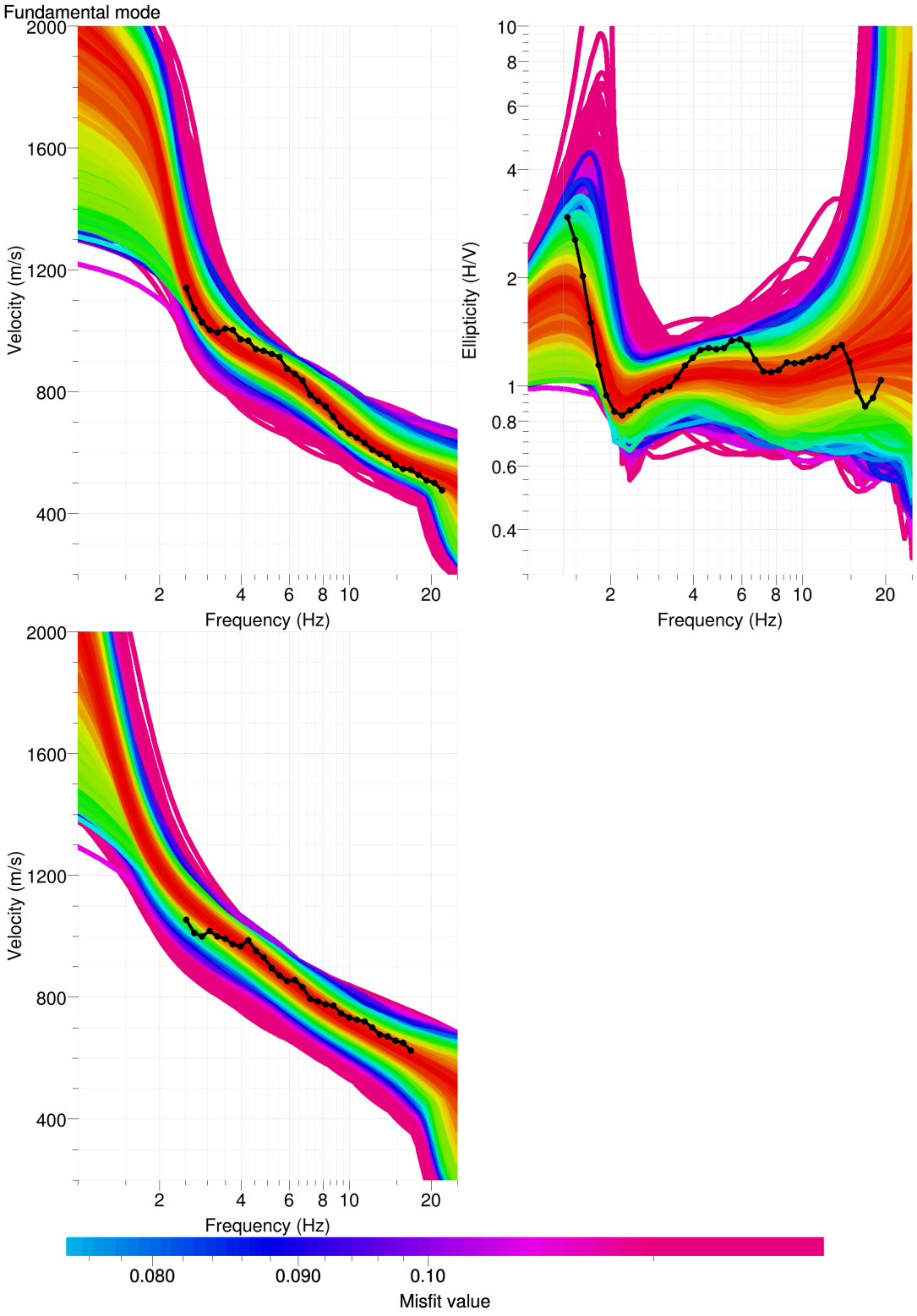

Figure 19: Comparison between inverted models and measured Rayleigh and Love modes and corresponding ellipticity, fixed layer depth strategy.

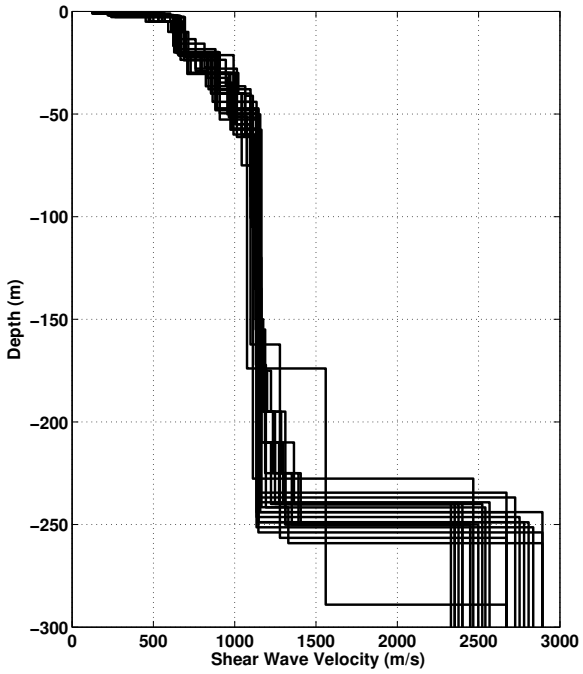

Figure 20: V_s ground profiles for the selected 25 best models.

7.2 Travel time average velocities and ground type

The distribution of the travel time average velocities at different depths was computed from the selected models. The uncertainty, computed as the standard deviation of the distribution of travel time average velocities for the considered models, is also provided, but its meaning is doubtful. $V_{s,30}$ is found to be $620\,\mathrm{m/s}$, which corresponds to class B in the Eurocode 8 [CEN, 2004] and SIA261 [SIA, 2003]. The map of foundation classes on the website `http://map.bafu.admin.ch/` is providing a class C at this site. This measurement shows the sediments are more consolidated than expected.

7.3 SH transfer function and quarter-wavelength velocity

The quarter-wavelength velocity approach [Joyner et al., 1981] provides, for a given frequency, the average velocity at a depth corresponding to 1/4 of the wavxelength of interest. It is useful to identify the frequency limits of the experimental data (minimum frequency in dispersion curves at $2.5\,\mathrm{Hz}$ and the ellipticity peak at $1.34\,\mathrm{Hz}$ here). The results using this proxy show that the dispersion curves constrain the profiles down to $85\,\mathrm{m}$ and the ellipticity down to $180\,\mathrm{m}$ (Fig. 21). Moreover, the quarter wavelength impedance-contrast introduced by Poggi et al. [2012] is also displayed in the figure. It corresponds to the ratio between two quarter-wavelength average velocities, respectively from the top and the bottom part of the velocity profile, at a given frequency [Poggi et al., 2012]. It shows a trough (inverse shows a peak) at the resonance

	Mean (m/s)	**Uncertainty (m/s)**
$V_{s,5}$	367	24
$V_{s,10}$	468	20
$V_{s,20}$	551	17
$V_{s,30}$	620	15
$V_{s,40}$	675	14
$V_{s,50}$	723	10
$V_{s,100}$	876	9
$V_{s,150}$	948	9
$V_{s,200}$	994	7

Table 7: Travel time averages at different depths from the inverted models. Uncertainty is given as one standard deviation from the selected profiles.

frequency.
Moreover, the theoretical SH-wave transfer function for vertical propagation [Roesset, 1970] is computed from the inverted profiles. It is compared to the quarter-wavelength amplification [Joyner et al., 1981] that however cannot take resonances into account (Fig. 22). In this case, the models are predicting a moderate amplification up to a factor of 3 at the resonance peaks at 1.24, 3.35, 5.3, $7.3\,\mathrm{Hz}$ etc.

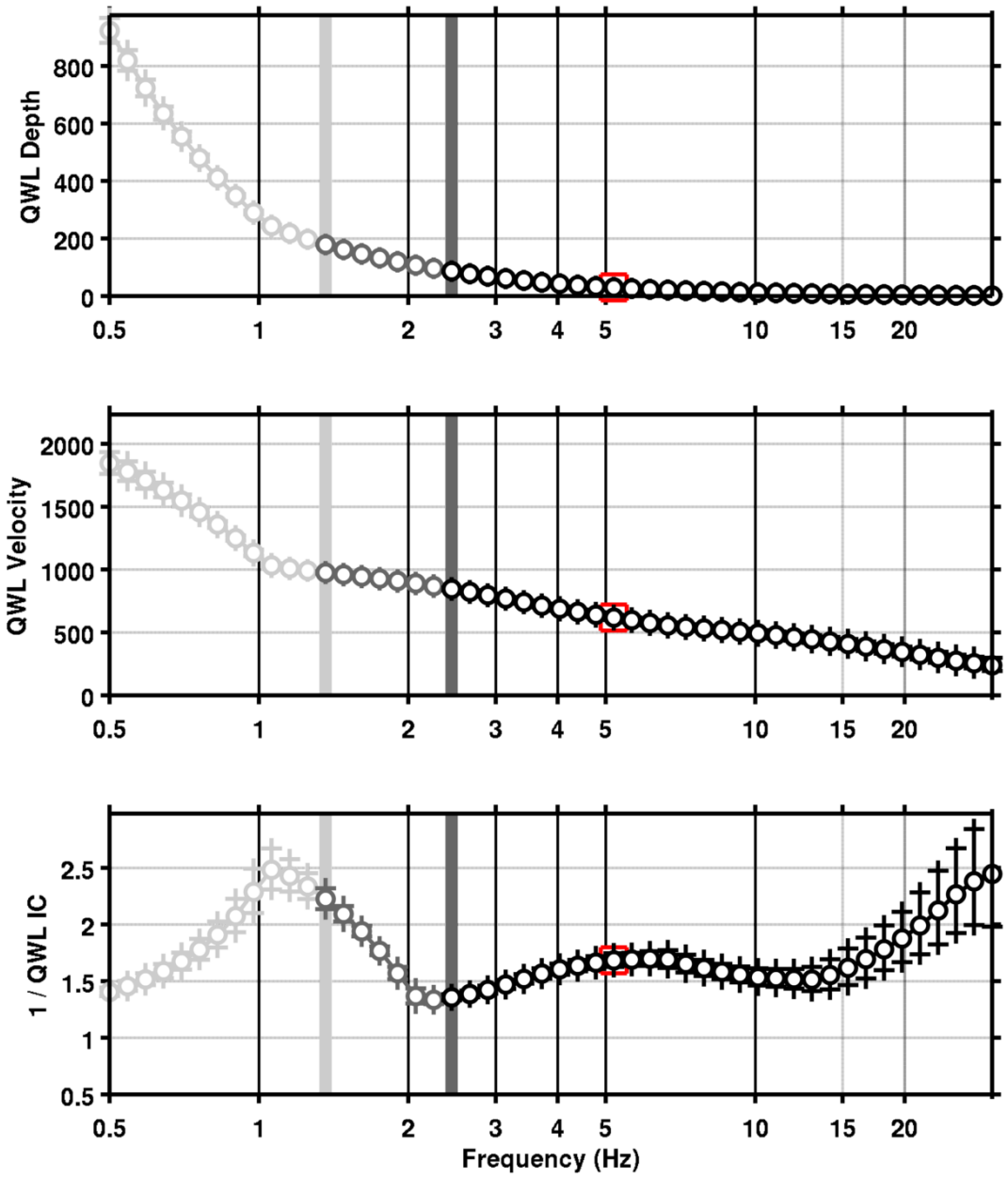

Figure 21: Quarter wavelength velocity representation of the velocity profile (top: depth, centre: velocity, bottom: inverse of the impedance contrast). Black curve is constrained by the dispersion curves, light grey is not constrained by the data. Red square is corresponding to $V_{s,30}$.

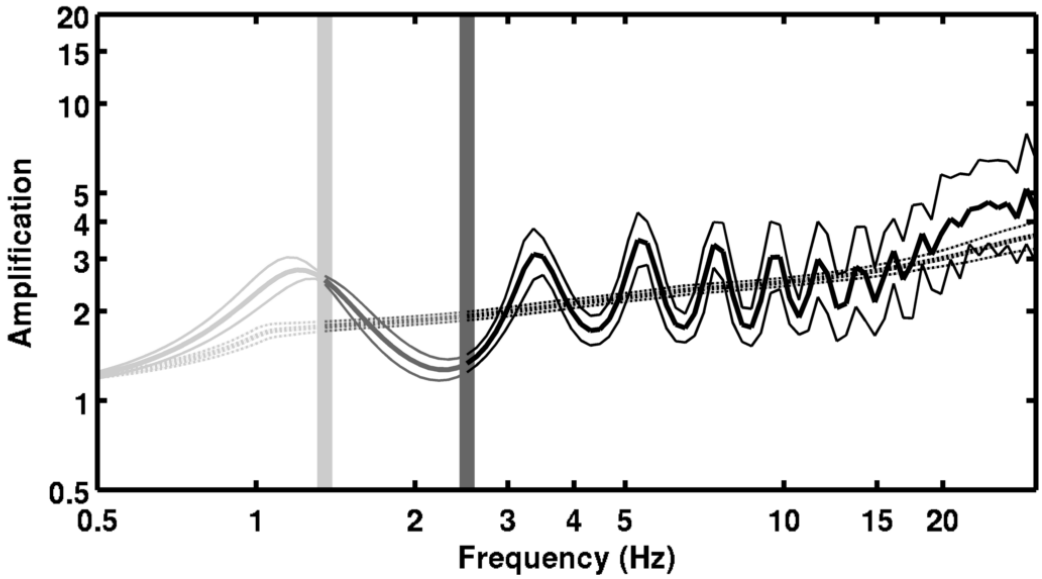

Figure 22: Theoretical SH transfer function (solid line) and quarter wavelength impedance contrast (dashed line) with their standard deviation. Significance of the greyshades is detailed in Fig. 21.

8 Conclusions

Ambient vibration array measurement in Linthal allowed to derive important properties of the ground structure allowing to invert from the soil velocity profile. The investigated site is finally mostly 1D. Rayleigh and Love fundamental modes could be extracted on a broad frequency band.
The narrow alpine valley in Linthal is hosting a relatively deep basin (about $250\,\mathrm{m}$ here). The filling is however made of stiff sediments with velocities from 600 up to $1100\,\mathrm{m/s}$. A thin layer at the surface of 2 to $3\,\mathrm{m}$ depth with low velocity (200 to $300\,\mathrm{m/s}$) is inverted. Down to $20\,\mathrm{m}$ depth, the velocity remains between 600 and $700\,\mathrm{m/s}$ but then starts to increase linearly with depth down to $60\,\mathrm{m}$ depth where it reaches velocities around $1100\,\mathrm{m/s}$. This velocity seems to stay constant until the bedrock, at a depth of about $250\,\mathrm{m}$ with a velocity found between 2400 and $2900\,\mathrm{m/s}$ (hardly constrained). $V_{s,30}$ is found to be $620\,\mathrm{m/s}$, corresponding to class B in the Eurocode 8. Amplification is found to be up to 3 at the resonance peaks.

Acknowledgements

The author thanks Marko Terzic and Kees Weemstra for the help during these measurements.

References

Pierre-Yves Bard and Michel Bouchon. The Two-dimensional resonance of sediment-filled valleys. *Bulletin of the Seismological Society of America*, 75(2):519–541, 1985.

Sylvette Bonnefoy-Claudet, Fabrice Cotton, and Pierre-Yves Bard. The nature of noise wavefield and its applications for site effects studies. *Earth-Science Reviews*, 79(3-4): 205–227, December 2006. ISSN 00128252. doi: 10.1016/j.earscirev.2006.07.004. URL http://linkinghub.elsevier.com/retrieve/pii/S0012825206001012.

Jan Burjánek, Gabriela Gassner-Stamm, Valerio Poggi, Jeffrey R. Moore, and Donat Fäh. Ambient vibration analysis of an unstable mountain slope. *Geophysical Journal International*, 180(2):820–828, February 2010. ISSN 0956540X. doi: 10.1111/j.1365-246X.2009.04451.x. URL http://doi.wiley.com/10.1111/j.1365-246X.2009.04451.x.

J. Capon. High-Resolution Frequency-Wavenumber Spectrum Analysis. *Proceedings of the IEEE*, 57(8):1408–1418, 1969.

CEN. *Eurocode 8: Design of structures for earthquake resistance - Part 1: General rules, seismic actions and rules for buildings*. European Committee for Standardization, en 1998-1: edition, 2004.

Benjamin Edwards, Clotaire Michel, Valerio Poggi, and Donat Fäh. Determination of Site Amplification from Regional Seismicity: Application to the Swiss National Seismic Networks. *Seismological Research Letters*, 84(4):611–621, July 2013. ISSN 0895-0695. doi: 10.1785/0220120176. URL http://srl.geoscienceworld.org/cgi/doi/10.1785/0220120176.

Donat Fäh, Fortunat Kind, and Domenico Giardini. A theoretical investigation of average H / V ratios. *Geophysical Journal International*, 145:535–549, 2001.

Donat Fäh, Gabriela Stamm, and Hans-Balder Havenith. Analysis of three-component ambient vibration array measurements. *Geophysical Journal International*, 172(1):199–213, January 2008. ISSN 0956540X. doi: 10.1111/j.1365-246X.2007.03625.x. URL http://doi.wiley.com/10.1111/j.1365-246X.2007.03625.x.

Donat Fäh, Marc Wathelet, Miriam Kristekova, Hans-Balder Havenith, Brigitte Endrun, Gabriela Stamm, Valerio Poggi, Jan Burjanek, and Cécile Cornou. Using Ellipticity Information for Site Characterisation Using Ellipticity Information for Site Characterisation. Technical report, NERIES JRA4 Task B2, 2009.

William B. Joyner, Richard E. Warrick, and Thomas E. Fumal. The effect of Quaternary alluvium on strong ground motion in the Coyote Lake, California, earthquake of 1979. *Bulletin of the Seismological Society of America*, 71(4):1333–1349, 1981.

Katsuaki Konno and Tatsuo Ohmachi. Ground-Motion Characteristics Estimated from Spectral Ratio between Horizontal and Vertical Components of Microtremor. *Bulletin of the Seismological Society of America*, 88(1):228–241, 1998.

Valerio Poggi and Donat Fäh. Estimating Rayleigh wave particle motion from three-component array analysis of ambient vibrations. *Geophysical Journal International*, 180(1):251–267, January 2010. ISSN 0956540X. doi: 10.1111/j.1365-246X.2009.04402.x. URL http://doi.wiley.com/10.1111/j.1365-246X.2009.04402.x.

Valerio Poggi, Benjamin Edwards, and D. Fah. Characterizing the Vertical-to-Horizontal Ratio of Ground Motion at Soft-Sediment Sites. *Bulletin of the Seismological Society of America*, 102(6):2741–2756, December 2012. ISSN 0037-1106. doi: 10.1785/0120120039. URL http://www.bssaonline.org/cgi/doi/10.1785/0120120039.

J.M. Roesset. Fundamentals of soil amplification. In R. J. Hansen, editor, *Seismic Design for Nuclear Power Plants*, pages 183–244. M.I.T. Press, Cambridge, Mass., 1970. ISBN 978-0-262-08041-5. URL http://mitpress.mit.edu/catalog/item/default.asp?ttype=2\&tid=5998.

Daniel Roten, Donat Fäh, Cécile Cornou, and Domenico Giardini. Two-dimensional resonances in Alpine valleys identified from ambient vibration wavefields. *Geophysical Journal International*, 165(3):889–905, June 2006. ISSN 0956540X. doi: 10.1111/j.1365-246X.2006.02935.x. URL http://doi.wiley.com/10.1111/j.1365-246X.2006.02935.x.

SIA. *SIA 261 Actions sur les structures porteuses*. Société suisse des ingénieurs et des architectes, Zürich, sia 261:20 edition, 2003.

Marc Wathelet. An improved neighborhood algorithm: Parameter conditions and dynamic scaling. *Geophysical Research Letters*, 35(9):1–5, May 2008. ISSN 0094-8276. doi: 10.1029/2008GL033256. URL http://www.agu.org/pubs/crossref/2008/2008GL033256.shtml.